Diffusion of Polymers at Interfaces: A Secondary Ion Mass Spectroscopy Study†

Scott J. Whitlow and Richard P. Wool*

Department of Materials Science and Engineering, University of Illinois, 1304 West Green Street, Urbana, Illinois 61801

Received July 12, 1990; Revised Manuscript Received July 2, 1991

ABSTRACT: Secondary ion mass spectroscopy (SIMS) was used to measure depth profiles $c(x,t)$ at symmetric deuterated (DPS)–protonated (HPS) polystyrene interfaces as a function of temperature T and molecular weight M. The self-diffusion coefficient D was obtained from $c(x,t)$ with a depth resolution of ca. 130 Å, using the Matano–Boltzmann method. By using molecular weights with $M = 10^6$, it was possible to test scaling laws for interdiffusion predicted by the de Gennes reptation model at $t < \tau$ (reptation time) and distances $x < R_G$ (radius of gyration). The following results were obtained. At times $t > \tau$, $D \propto M^{-2}$; at $t < \tau$, the apparent D value was much greater than the equilibrium long time value. This effect is due to Rouse segmental motion and not center of mass motion. At $t < \tau$, the number of monomers crossing the interface $N(t)$ and the average monomer interpenetration distance $X(t)$ were determined from $c(x,t)$ as $N \propto t^{3/4}$ and $X(t) \propto t^{1/4}$, in agreement with the reptation theory. At $t > \tau$, both $N(t)$ and $X(t)$ increased with a $t^{1/2}$ dependence; the crossover in scaling laws occurred approximately at τ. The temperature dependence of D was well described by the Vogel analysis. Thermodynamic slowing down of the diffusion coefficient due to the deuterium isotope effect was considered to be minimal in the distance range explored by the SIMS method, $x < 500$ Å. The SIMS results were in agreement with similar studies using neutron reflection.

Introduction

Information about the diffusion properties of polymers is essential for many technological applications. Examples include mechanical property control in welded and melt-processed polymers, molding and sintering of pellets, and autohesion of elastomers. On a more fundamental level, molecular theories of polymer dynamics require experimental support for verification. The needs and requirements of both areas provide an impetus for the refinement of experimental techniques used to measure the dynamics of polymer diffusion. The reptation dynamics model[1-5] recognizes that entanglements have an effect on polymer diffusion and viscoelastic properties. In this model, the polymer chain is constrained by its neighbors to motion along a tube defined by its contour. The important distance scale of motion in the reptation regime is quite small, on the order of the random-coil radius of gyration, R_g. Investigation of the reptation model at interfaces requires an experimental technique with an important property: the depth resolution capability to measure small-scale diffusion depths ($x < R_g$).

Recent techniques for measuring depth profiles include forward recoil spectroscopy (FRES),[6,7] infrared (IR) spectroscopy,[8,9] small-angle neutron scattering (SANS),[10,11] and specular neutron reflection (SNR).[12-14] IR and attenuated total reflectance (ATR) IR are limited by a depth resolution of about 1000–10 000 Å but provide useful information at large interdiffusion depths. FRES, SANS, and SNR do not measure depth profiles directly, and assumptions must be made about the nature of the profile before it can be constructed from the raw data. FRES has been used successfully to explore long-range interdiffusion, particularly using polystyrene interfaces. SNR has been developed to examine short-range interdiffusion in polymers with a resolution of about 5–10 Å. Secondary ion mass spectroscopy (SIMS) is another technique for measuring polymer diffusion and has been used by us recently to examine interdiffusion in polystyrene interfaces.[15] SIMS has a high sensitivity to hydrogen and deuterium, making it useful for tracer studies, and has the ability to measure depth profiles directly. In addition, this technique can monitor elements to much greater depths than some of the above methods. While it provides the concentration profile directly, its depth resolution, which is about 100 Å for polymers, is not as good as the SNR technique with a resolution of about 5 Å. However, useful information can be obtained at distances less than the random-coil size by using high molecular weight polymers, as we demonstrate herein.

In this paper, we further develop the SIMS method for analyzing polymer interfaces and explore the short-range dynamics of polystyrene chains. The exploration of the short-range dynamics of polymer chains at interfaces represents a critical test of the reptation model where a crossover in the time dependence of several scaling laws occurs at the reptation time. The temperature dependence of the self-diffusion coefficients and the thermodynamics of interaction of HPS with DPS are also examined.

Theoretical Considerations

Reptation and Minor Chain Models. Polymers in a concentrated solution and melt are in a highly entangled state. Neighboring chains are obstacles, restricting motion of the polymer chain to a tube where curvilinear one-dimensional diffusion occurs along its contour, as shown in Figure 1. Random motion occurs in both directions along the tube. Memory of the initial tube configuration is gradually lost because motion of the chain ends is random. The chain is always restricted to movement in a tube, but only the central portion remains in the initial tube for times less than the reptation time, τ. The part that escapes from the initial tube is a random coil called the minor chain.[17,18] This segment obeys Gaussian statistics, and a spherical envelope can be used to represent its static dimensions. The evolution of the minor chains at a polymer–polymer interface provides a convenient

* Author to whom correspondence should be addressed.
† Paper presented at the American Physical Society, St. Louis, MO, March 1989.

0024-9297/91/2224-5926$02.50/0

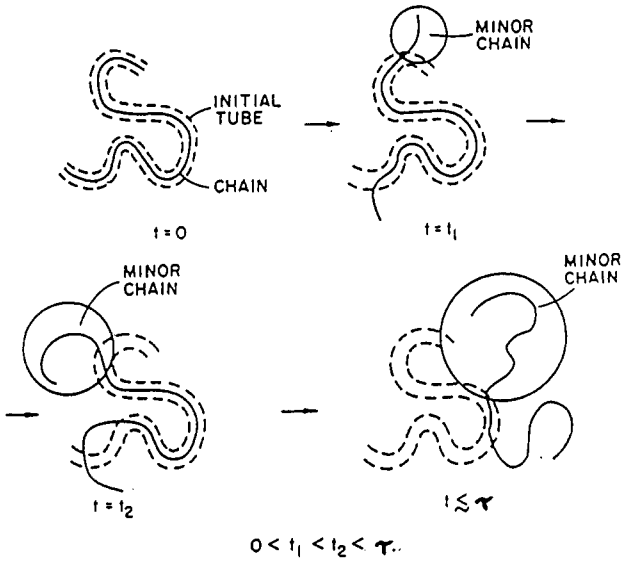

Figure 1. Growth of a minor chain as polymer reptates out of its initial tube. The spherical envelope surrounding the minor chain describes the random-coil dimensions and most probable location.

Table I
Minor Chain Properties

property	symbol	dynamic relation $t < \tau$	dynamic relation $t > \tau$
no. of monomers crossing interface[b]	N	$t^{3/4}M^{-7/4}$	$t^{1/2}M^{-1}$
av interpenetration depth	$\bar{X}$	$t^{1/4}M^{-1/4}$	$t^{1/2}M^{-1}$
center of mass	x_{cm}	$t^{1/2}M^{-1}$	$t^{1/2}M^{-1}$
no. of chains[b]	n	$t^{1/4}M^{-5/4}$	$t^{1/2}M^{-2}$
no. of bridges[b]	p	$t^{1/2}M^{-3/2}$	$t^{0}M^{0}$
av contour length	l	$t^{1/2}M^{-1/2}$	$t^{0}M^{1}$
general property[a]	H'	$t^{r/4}M^{-s/4}$	

[a] $r, s = 1, 2, 3, \ldots$. [b] Assumes uniform chain end distribution.

method of determining molecular properties and concentration profiles.

The minor chains grow with time, and eventually the whole chain escapes from its initial configuration at the reptation time, τ. Calculations based on the minor chain reptation model have been used to develop scaling laws (Table I) for polymer interfaces.[18,21] For example, the number of monomers $N(t)$ crossing a symmetric amorphous interface as a function of time t and molecular weight M is described by

$$N(t) \propto t^{3/4}M^{-7/4} \quad (t < \tau) \tag{1}$$

$$N(t) \propto t^{1/2}M^{-1} \quad (t > \tau) \tag{2}$$

Equations 1 and 2 can be derived from first principles[21] as well as through the use of scaling.[20,22,23] A second important minor chain property is the average monomer interpenetration depth $X(t)$, given by

$$X(t) \propto t^{1/4}M^{-1/4} \quad (t < \tau) \tag{3}$$

$$X(t) \propto t^{1/2}M^{-1} \quad (t > \tau) \tag{4}$$

At $t = \tau$, $X(t) \approx R_g$. Other minor chain scaling laws are listed in Table I.[17] When $N(t)$ and $X(t)$ are known, all other relations can be derived.

The number of monomers $N(t)$ and the average monomer interdiffusion distance $X(t)$ can be measured experimentally from the depth profile $c(x,t)$ by using

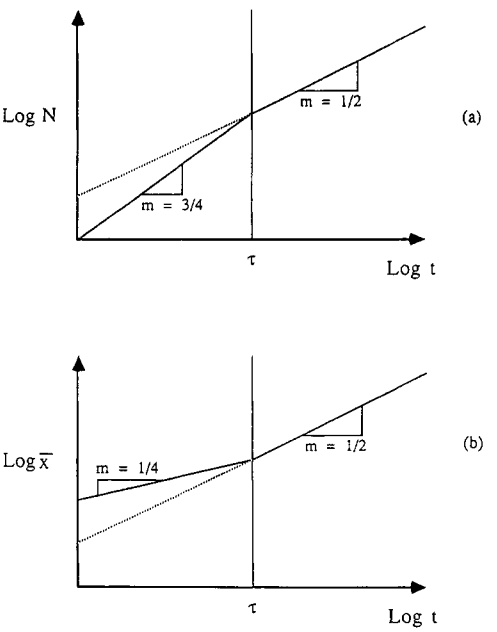

Figure 2. Qualitative transition prediction at the reptation time, τ, for (a) the number of monomers crossing the interface, N, and (b) the average interpenetration distance, X.

$$N(t) = \int_0^\infty c(x,t)\,dx \tag{5}$$

$$X(t) = \frac{\int_0^\infty xc(x,t)\,dx}{\int_0^\infty c(x,t)\,dx} \tag{6}$$

Here $N(t)$ is obtained from the area under the profile, and $X(t)$ is measured from its normalized first moment. Depth profiles of bilayer samples healed at $t < \tau$ and $t > \tau$ can be used to evaluate scaling laws for $N(t)$ and $X(t)$ as shown schematically in Figure 2. The simultaneous crossover in slopes from $^3/_4$ to $^1/_2$ for $N(t)$ and from $^1/_4$ to $^1/_2$ for $X(t)$ at the reptation time is highly characteristic of the reptation theory.

Measurement of Diffusion. The fundamental equation for the study of isothermal diffusion is Fick's second law

$$\frac{\partial c}{\partial x} = \frac{\partial}{\partial x}\left(D\frac{\partial c}{\partial x}\right) \tag{7}$$

where the diffusion coefficient D may vary with concentration or it can be constant. The Matano–Boltzmann method[25,26] is the approach commonly used with a concentration-dependent diffusion coefficient, and the Grube method[25] is used when D is independent of concentration. The latter approach can be used when D is a weak function of composition.

The solution to Fick's second law with D as a constant (Grube method) results in a closed-form error-function solution. The Matano–Boltzmann method necessitates a solution to eq 7 in the form

$$\frac{\partial c}{\partial t} = \frac{\partial}{\partial x}\left[D(c)\frac{\partial c}{\partial x}\right] \tag{8}$$

The analysis is more complex when D is not constant. This solution for the diffusion coefficient is

$$D = -\frac{1}{2t}\frac{\partial x}{\partial c}\int_{c_0}^{c} dc \tag{9}$$

which requires a numerical or graphical analysis. The

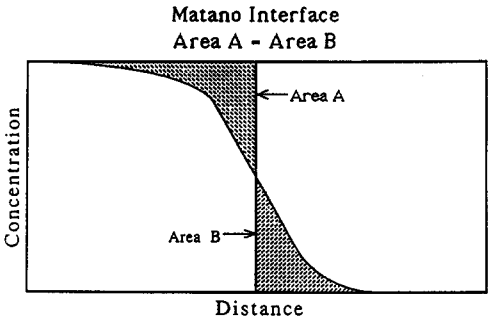

Figure 3. Position of the Matano interface.

Matano interface (Figure 3) must first be located before eq 9 can be employed. The point where the diffusant areas A and B are equal identifies the Matano interface at $x = 0$. The maximum in the profile derivative locates the Matano interface for the symmetric case. Polymer diffusion coefficients can be functions of composition as demonstrated by Kramer et al.,[27] which justifies the use of the Matano–Boltzmann approach over the Grube method. Additional problems can develop with the use of deuterated polymers, which results in immiscibility[31] and thermodynamic slowing down (TSD) due to the deuterium isotope effect.[33,34]

Temperature Dependence of Diffusion. The temperature dependence of the diffusion coefficient D can be described by two approaches. The first is the Arrhenius activation energy process given by

$$D = D_0 \exp(-Q/RT) \tag{10}$$

where Q is the activation energy and D_0 is a pressure-dependent constant. The second is an empirical approach given by the Vogel relation

$$\log (D/T) = A - B/(T - T_\infty) \tag{11}$$

For polystyrene with a number-average molecular weight $M = 255\,000$ (255K), $A = -9.49$,[28,29] $B = 710$, and $T_\infty = 322$ K = 49 °C. The empirical constant A has a molecular weight dependence given by

$$A = -9.49 - 2 \log (M/255\text{K}) \tag{12}$$

The temperature range for eq 11 with these values is 120–219 °C[33] while the Arrhenius law is most useful for high temperatures ($T > 155$ °C).

Thermodynamics of Interaction. Many analytical methods used in the study of polymer diffusion rely on isotopic labeling.[6-15] All of the approaches assume that polymers and their chemically identical deuterated analogues form ideal solutions. Recent results from SANS[31,32] and FRES[33,34] measurements indicate that binary mixtures of normal and deuterated polystyrenes are characterized by a small, but positive, Flory–Huggins interaction parameter, χ.

Phase equilibrium and mutual diffusion will be affected by a positive χ. The mutual diffusion coefficient should undergo a "thermodynamic slowing down" in the proximity of the critical composition c_{cr} where

$$c_{cr} = N_H^{1/2}/[N_H^{1/2} + N_D^{1/2}] \tag{13}$$

The diffusion coefficient for a blend is given by[27]

$$D = \Omega(c)\,[\chi_s(c) - \chi] \tag{14}$$

where

$$\chi_s = \frac{1}{2}\left\{\frac{1}{N_D c} + \frac{1}{N_H(1-c)}\right\} \tag{15}$$

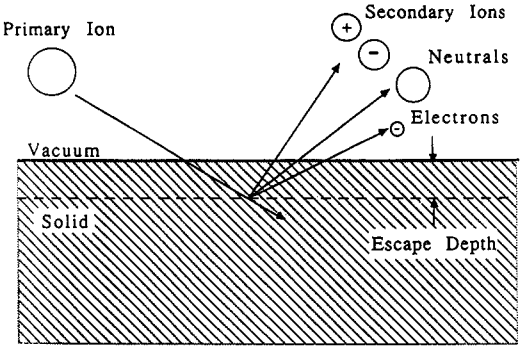

Figure 4. Schematic of the sputtering process caused by an impinging primary ion resulting in secondary ions, neutral atoms, and electrons.

and

$$\Omega(c) = 2c[D^*_D N_D(1-c) + D^*_H N_H c] \tag{16}$$

The χ term in eq 14 corrects the χ_S term for noncombinatorial entropy of mixing and (positive) enthalpic contributions to the thermodynamic driving force. Thermodynamic slowing down should be more pronounced as χ approaches $\chi_S(c)$ or, alternatively, as the temperature approaches the upper critical solution temperature (UCST).[33] When χ nears zero or at temperatures sufficiently far from the critical point, thermodynamic slowing down should not be observed.[32] However, the distance scale ($x < 500$ Å) investigated in the SIMS study may be too short to allow the large-scale concentration fluctuations to develop and promote the TSD effect.

Secondary Ion Mass Spectroscopy

The basis for SIMS is the ejection of charged atoms and molecules caused by an impinging ion beam (Figure 4). The primary ion beam is rastered over a selected region to erode the sample surface.[35-37] Charged species are filtered and then detected by a mass spectrometer tuned to an element of interest at that depth. The present discussion will concentrate on a brief review of the SIMS process as it is used for depth profiling. References are available with details on SIMS,[35-37] other surface characterization techniques,[37,38] and the fundamentals of sputtering.[40,41]

Impingement of energetic ions affects the sample surface in two ways. The first effect is a loss of surface material known as sputtering. The second effect involves changes in the target structure known as atomic mixing. In depth profiling, sputtering is desirable whereas atomic mixing results in a loss of depth resolution.

Sputtering. The sputtering process is shown schematically in Figure 4. The incoming ion dissipates a large portion of its energy in the vicinity of the sample surface, transferring energy and momentum to a region around the point of impact. Target atoms within a certain (escape) depth have enough kinetic energy to overcome the surface potential and eject from the sample. The escape depth is usually quite small, typically only a few monolayers. Most sputtered species are neutral, although a small number undergo charge exchange with their local environment, producing positive and negative secondary ions (secondary current). The primary ion beam current is held constant, and the secondary current is measured as a function of time.

Several approaches are available for the quantitative analysis of raw profiles.[36,42,43] The secondary ion current is usually converted to an absolute concentration by the use of standards. The present study employs diffusion

couples where the concentration of deuterium varies from 100% to essentially zero. Since only relative differences in concentration are important, there is no need to convert the secondary ion current to an absolute concentration. There are several methods for calibrating the depth scale. The procedure used for this study will be discussed in a later section.

Sputtered particles may be atoms or molecules. The number and type increase with decreasing primary ion current density. This fact has been used to characterize polymer surfaces in the static (low-energy) SIMS mode.[44] Depth profiling requires energies in the dynamic SIMS mode ($jp \geq 10$ nA/cm^2). Dynamic and static SIMS has long been an important tool for the analysis of semiconductors. However, relatively little work has been done on depth profiling of polymers.[12,46,47]

Atomic Mixing. Two principal contributions to atomic mixing are recoil implantation and cascade mixing. For a given primary ion energy, the energy transferred from the primary ion to the target atom depends on the distance of closest approach known as the impact parameter, P. For atoms of comparable mass, recoil implantation will occur when the impact parameter is small. The collision is similar to that between two billiard balls. The primary ion will elastically transfer a significant portion of its energy and momentum. Consequently, the target atom will recoil deep into the sample. Large impact parameter collisions produce cascade mixing. Less energy is transferred to the target atom because the interaction between the ion and target atom now involves a screened Coulombic potential in place of the hard-sphere potential active for recoil implantation. Instead of recoiling into the sample, the target atom displaces its neighboring atoms, producing secondary cascades. There is a general homogenization of the near-surface atoms affected by the cascade.

The probability of transferring a given amount of energy is usually expressed in terms of the area through which an ion trajectory must pass. This area is called the differential stopping cross section and is given in terms of the impact parameter P as

$$d\sigma = 2\pi P\, dP \tag{17}$$

Obviously, the probability for energy transfer increases with increasing impact parameter. Consequently, cascade mixing will be more probable than recoil implantation and will be the dominant contribution to atomic mixing.

The thickness of the region affected by atomic mixing is usually on the order of the primary ion range.[36] This parameter characterizes the distribution of depths where primary ions lose all of their energy. Primary ion acceleration voltage and masses of the interacting species are factors that influence the primary ion range for a given target. Monte Carlo (TRIM 86) and molecular dynamic[42] programs are available for calculating primary ion ranges as well as other parameters of interest in ion beam interactions. These programs can be used to evaluate the effects of different primary ions and experimental conditions.

Distortion of Depth Profile. Atomic mixing has the adverse effect of broadening an initially sharp interface (Figure 5a) given by the step function $c(z)$. The measured profile is given by the secondary ion current $I(z)$. Broadening of the measured profile relative to the ideal profile is quantified by the depth resolution, Δz (Figure 5a). There are several definitions of Δz, but the most common is the depth range where the signal drops from 84% to 16% of the maximum secondary ion current.[36,37] This is an arbitrary definition that corresponds to twice the standard deviation of the resolution or response function. The

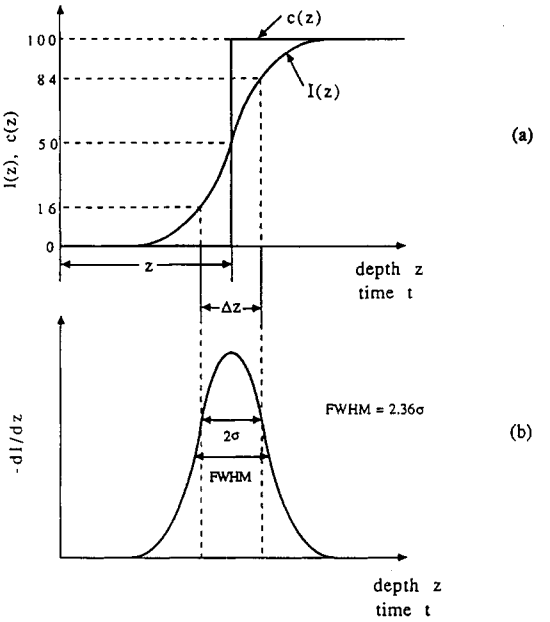

Figure 5. Broadening (a) of the measured profile, $I(z)$, relative to the initial step profile, $c(z)$, quantified by the depth resolution, $v(z)$. The measured profile is a convolution of the true profile with the response function (b). In most cases, the response function is the (negative) derivative of $I(z)$ measured for a sharp interface.

resolution function accounts for all effects that distort a measured profile compared to its true profile. Instrumental effects as well as sample–instrument interaction are included. The response function is assumed to be Gaussian and independent of sputtering depth. When the true profile is a step function, the response function is found as the derivative of the measured profile.[37]

The optimal depth resolution is determined by the atomic mixing range and, hence, the primary ion range.[36] Atomic mixing dominated by cascade mixing will depend on the primary ion energy, atomic numbers of the interacting species, and the angle between the primary beam and the sample surface. Low-energy, high atomic number ions at small ion beam to sample surface angles can be used to minimize atomic mixing.[37,48,50-53] There are a number of other effects that can severely degrade the optimal depth resolution for a given sample–instrument system. These artifacts can be divided into instrumental factors and ion matrix effects.[37,54] Instrumental factors depend on the particular SIMS being utilized. Ion matrix effects include selective sputtering, initial surface roughness, and sample charging. Selective sputtering is a problem only for multielemental targets whose components have significantly different sputter yields. Fortunately, selective sputtering is not an issue in the present work; the sputtering rates for hydrogen, deuterium, and carbon are slightly different, but the differences are small. SEM micrographs of bilayers that were not completely sputtered through to the silicon substrate did not exhibit cones or other selective sputtering artifacts. Exceptional care must be taken to make sure the sample surface is flat, especially with procedures employed for making polymer diffusion couples. On a rough surface, a uniform sputtering rate will produce signals simultaneously from different depths, hence, degrading the depth resolution.

Polymers are insulators, and they charge when bombarded with ions. Secondary electrons lost during sputtering leave a net positive charge on the specimen,[36] and interactions between the secondary ions and the matrix are adversely effected. Several approaches have been used

Table II
Material Characterization Data[a]

polym	mol wt (M_w)	polydispersity index (M_w/M_n)	degree of polymzn (N_D or N_H)	monomer ratios N_D/N_H
DPS	1082K	1.07	9031	
HPS	929K	1.10	8121	1.11
DPS	693K	1.03	6007	
HPS	591K	1.06	5361	1.12
DPS	203K	1.03	1726	
HPS	169K	1.06	1533	1.12
DPS	111K	1.05	943	
HPS	93K	1.06	921	1.02

[a] Molecular weight measurements by laser light scattering.

to solve this problem,[35] including gold coating, flooding the sputtered area with electrons, and the use of conductive masks and grids. Another approach is to change the sample surface potential during data acquisition, which can be quite difficult in practice.

Experimental Procedure

Materials. The samples consisted of symmetric bilayers of deuterated and hydrogenated polystyrene films. Characterization data are listed in Table II. The deuterated polystyrenes (DPS) were obtained from Polymer Laboratories, and the hydrogenated polystyrenes (HPS) were obtained from Pressure Chemical Co. Solutions of each were made with reagent-grade toluene. Concentrations for the HPS and DPS solutions were 0.04 and 0.01 g/mL, respectively. The term symmetric denotes matching the bilayer films on a degree of polymerization basis. For commercially available polystyrenes the best match possible for each bilayer was $N_D/N_H \approx 1.10$.

There are three reasons for choosing polystyrene as the material for this experiment. First, polystyrene is made by anionic polymerization, which helps ensure that molecular weight distributions are narrow. Second, atactic polystyrene is amorphous, making PS well suited for studying the dynamics of random-coil chains. A crystalline material would have additional diffusion mechanisms available, and there would be problems with channeling the primary ion beam during testing. Finally, PS is a well-characterized material for studying many aspects of polymer science, and comparison with diffusion results obtained by other workers, as reviewed in ref 55 and 56, is facilitated.

Sample Preparation. HPS layer: Silicon substrates, measuring 1.8 cm × 0.8 cm, were cut from a large wafer. The substrates were cleaned using the standard RCA method for electronic device preparation,[57] which is essentially a three-step process. The substrate is initially washed in reagent-grade acetone and then washed in reagent-grade isopropyl alcohol, followed by a rinse in deionized water. Substrates are then heated at 120 °C for 15 min in ambient atmosphere to remove any residual water. The RCA cleaning method ensures that the photoresist, used to protect the wafer surface during cutting, and silicon dust are removed from the substrate before further processing.

A 45-mL volume of HPS solution was filtered through a 0.45-μm millipore system into a clean 100-mL graduated cylinder. The HPS film was solution cast onto the silicon by placing the substrate into the graduated cylinder for 10 min. A variable-speed motor, set at 20 rpm, was employed to dip and remove samples from the HPS solution at a constant rate. Upon removal from solution, each sample was held at the 100-mL mark on the graduated cylinder for about 3 min in order for the film to stabilize. A final step in HPS film preparation was the heat treatment to remove residual solvent. Samples, in a batch, are heated slowly to 120 °C, held for 6 h, and then cooled. Slow heating helps to avoid pinhole formation in the films.[57] A second benefit of the heat treatment is to remove residual stresses which arise during casting. The resulting average film thicknesses for dried HPS films were determined by ellipsometry and are given in Table III.

DPS layer: DPS solutions were filtered through a 0.45-μm millipore filter before processing. Microscope glass slides were cut into 1.5 cm × 1.5 cm squares and cleaned overnight in a chromic acid solution. The squares were cleaned by using the RCA method and then spun dry on a photoresist spinner. Approximately 40 μL of DPS solution was placed in the center of the slide. The square slide was spun at 2000 rpm for 40 s. Average thicknesses produced by this approach are given in Table III.

Table III
Average Bilayer Thickness

polymer pair	HPS layer, Å	DPS layer, Å	bilayer, Å
1082K DPS, 929K HPS	4227	1249	5476
693K DPS, 591K HPS	3530	1195	4725
203K DPS, 169 HPS	3026	1132	4158
111K DPS, 93K HPS	3026	1089	3539

Table IV
Optical Properties

material	real index n'	imaginary index k'
HPS and DPS	1.591	0
Au	0.250	3.46
SiO_2	1.523	0
Si	3.85	−0.2

Attempts at heat treating the DPS layers to remove orientation effects proved to be unsuccessful. A range of different heat treatments was employed to achieve annealing. All were unsuccessful because the DPS film adhered to the glass slide and could not be removed for further processing. This problem could be solved in principle by depositing the DPS film on a soluble smooth substrate, annealing the film, and dissolving the substrate.

Bilayers: After scoring the sides of the DPS square slides with a razor, the film was floated from the glass slide onto the surface of deionized water in a Petri dish. The DPS film was placed on the HPS film by manipulating the coated silicon substrates under the DPS film and lifting to form the bilayer. A batch of samples was prepared sequentially, using clean water and rinsing the Petri dish between samples.

Meticulous sample preparation was extremely important for this work because any dust or foreign matter absorbed onto the films severely degrades the depth resolution. Processing for all films and bilayers was conducted in a clean room to reduce airborne impurities. The RCA cleaning and water changing during this last step helped to minimize particle contamination.

Welding: After bilayer preparation, the batch was dried in a vacuum oven at room temperature for at least 72 h in order to remove water trapped between the layers. Samples were individually welded in a Mettler hot stage at controlled times and temperatures (±0.2 °C) to promote interdiffusion. Heat treatments were performed in a gaseous N_2 glovebox atmosphere to minimize the oxidized layer at the surface. During SIMS testing, the smaller oxidized layer helps to establish steady-state sputtering more quickly and a larger portion of the DPS layer plateau is observed before entering the transition (diffused) region.

Thickness measurement: After the sample thickness was measured by an L117 Gaertner manual ellipsometer. The basis for this technique is measuring the change in polarization of a laser beam after it has been reflected from the substrate surface.[58] The incident beam is linearly polarized, and the reflected beam is elliptically polarized. Phase and rotation shifts of the reflected beam are measured. These angles are used in the basic equations of ellipsometry to calculate optical properties and thickness. The Gaertner ellipsometer had a wavelength of 6328 Å. The polarizer and analyzer were both at 30° to the sample normal. Thickness measurements have an accuracy of ±20 Å, a significant improvement over the previously used stylus technique[15] with an accuracy of ±175 Å. Optical properties for polystyrene, silicon, glass, and gold are listed in Table IV.

Final sample preparation: The final step before SIMS testing involved coating the samples with a thin (≈200 Å) layer of gold to prevent charging. The gold-coating technique was the same as that used for the SEM observation. Samples were coated in a batch. A blank silicon substrate was included for subsequent gold thickness determination. The gold blank was a control,

Table V
Test Conditions

	primary beam	secondary beam
element	Cs^+	D^+, H^+, and C^+
accelerating voltage, kV	+12.66	+4.5 kV
current, nA	150	measd quantity

used to circumvent difficulties in thickness measurement that arise from an absorbing film (Au) on a transparent film (DPS + HPS).

Gold coating proved to be a superior method for preventing charging than application of an electron flood gun. Extensive damage to the region around the crater was observed after using an electron flood gun for charge compensation. It is believed that the flood gun causes electron-stimulated desorption. Secondary ions would be produced from the damaged surface region and the crater bottom simultaneously, degrading the depth resolution.

SIMS Testing. A Cameca IMS-3f secondary ion mass spectrometer was used to depth profile the HPS/DPS bilayers. The incoming primary beam, with a diameter of 60 μm, was rastered over a 500 μm × 500 μm area. Secondary ions were produced over the entire rastered area, but a mechanical aperture was used to monitor only a 60-μm circular area in the center of the crater.[15] Rastering promotes uniform sputtering within the analyzed area and promotes a flat crater bottom. Mechanical gating helps to prevent artifacts like memory effect and sputter redeposition from the crater edges.[50] Without rastering and gating, these artifacts would adversely affect the depth profile.

Testing conditions are listed in Table V. Observation of positive secondary ions requires a positive sample bias. The accelerating voltage for a positively charged primary ion will be reduced as it travels toward the sample. For the conditions in Table V, the relative accelerating voltage will be +8.16 kV, the difference between the primary ion accelerating voltage and the sample bias. In comparison, the observation of negatively charged ions would require a negative sample bias. For the same voltage magnitudes, the relative accelerating voltage would become +17.16 kV, double that for positive secondary ions. The primary ion range and atomic mixing effects would consequently extend over a greater distance, degrading the depth resolution.

Several types of primary beams were available on the Cameca IMS 3f: Cs^+, O_2^+, O^-, and Ar^+. Cesium has the greatest stopping power by virtue of its mass. Cesium also offers greater beam stability than the other choices. TRIM 86 (Transport of Ions in Matter) calculations show that Cs^+ at +8.16 kV has a much smaller penetration depth in PS (≈150 Å) than O^- or Ar^+ at the same energy (>275 Å). Extraction of cesium ions from its source in the primary beam column requires a minimum of +12.66 kV.

The positive carbon secondary current was measured to monitor the stability of the profile as shown in Figure 6. After steady-state sputtering is achieved, a constant C^+ current indicates that the testing is proceeding smoothly. Secondary currents for H^+ and D^+ are the measured quantities. The current intensities in Figure 6 are plotted in real time on a log intensity versus channel or cycle number (time unit) to facilitate quantitative analysis of depth profiles.

An important ion matrix effect in SIMS is mass interference, where signals from different atoms (or molecules) with the same mass-to-charge ratio interfere with one another. For example, a double-charged Si^{2+} atom (mass 28) would interfere with measuring Al^+ (mass 14). Control samples of hydrogenated, deuterated, and centrally deuterated triblock copolymer (D–H–D) were analyzed to evaluate H_2^+ interference with the D^+ signal. Results showed that H_2^+ interference was negligible, which is most likely attributable to its very low isotope abundance (0.015%). The large dynamic range of the deuterium signal, usually several decades (Figure 6), makes the D^+ signal less susceptible to H_2^+ interference.

During sample changes in the SIMS sample chamber, introduction of a small amount of water vapor is unavoidable. Hydrogen from the water interferes with the H^+ signal. The vacuum system (1×10^{-6} Torr) decreases the water vapor partial pressure as the test proceeds, resulting in a hydrogen signal that is a function of time. This effect is most clearly seen at the beginning of the depth profile as shown later. After sputtering through the initial surface layer (≈50 channels or 250 Å), the H^+ signal keeps decreasing. There is no steady-state sputtering before entering the transition zone. Uncertainty in the location of the lower H^+ plateau and its time-dependent nature render the hydrogen signal problematic for analysis. In this work, the concentration profiles were analyzed using the D^+ signal.

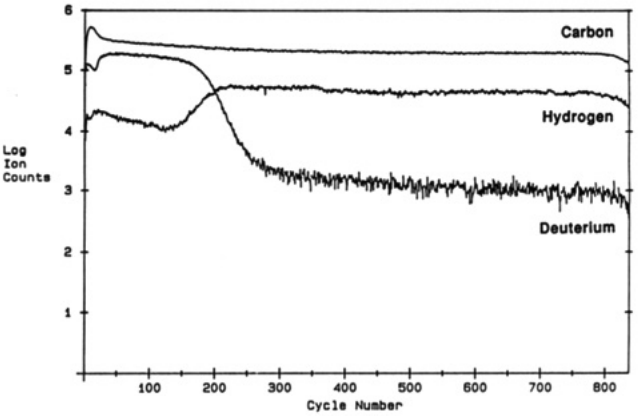

Figure 6. Raw profile from SIMS testing. This plot is the log secondary ion signal versus cycle number (time).

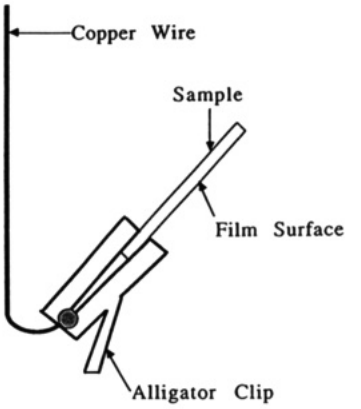

Figure 7. Holder and sample configuration for HPS film casting.

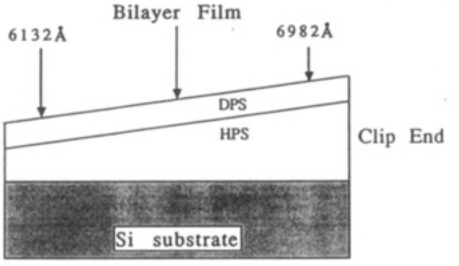

Figure 8. Thickness gradient for a sample induced by the HPS layer drying technique.

Methods of Data Analysis

Depth scale calibration: The HPS film casting technique (Figure 7) produces a thickness gradient as shown in Figure 8. The gradient occurs along the sample length, and thickness changes in the transverse direction are negligible. The spinning technique used for DPS produced uniform films. Consequently, the bilayer has the same thickness gradient as the HPS layer.

There are several methods for calibration of the depth scale.[36] Previous work[15] utilized a stylus technique to measure crater depth after testing. This approach introduces errors for polystyrene because the diamond-tipped stylus can have a variable penetration into the polymer during measurement. A second approach is to

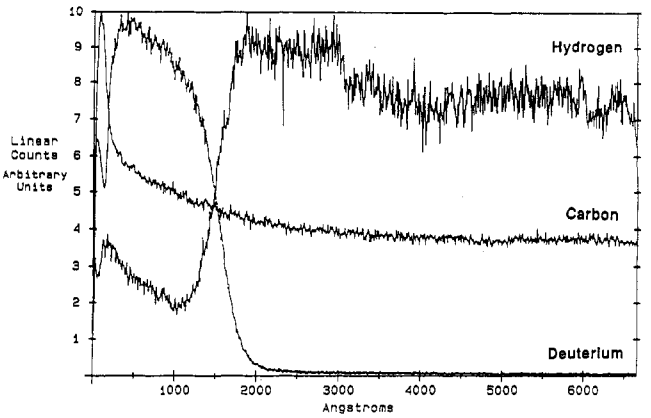

Figure 9. Figure 6 after depth scale calibration. The distance scale is in terms of sputter depth, z.

assume a constant sputter rate, z', such that the crater thickness is simply $z = z't$. Slight variation in the primary ion current during testing induces a great uncertainty in the depths found by this method.

The best approach for depth calibration of polymer samples is given as follows. Before Au coating, the gradient in thickness due to film casting in each sample is carefully measured by ellipsometry. The clip end of the sample is the datum for distance along the sample length. Thicknesses at several positions are analyzed to obtain the sample thickness gradient. Thicknesses at other positions were determined by linear interpolation. After SIMS testing, the distance of the center of each crater is measured with respect to the clip end. The gradient analysis was used to determine the precise bilayer thickness of each crater. Although the thickness gradient may be significant over the length of the sample, it becomes negligible over the 60-μm analyzed region. For example, one of the largest gradients measured was $\approx$1100 Å from sample end to end. The thickness change over the 60-μm analyzed area is then $\approx$4 Å. Therefore, the gradient is small enough that the depth resolution is unaltered, but it must be measured in order to determine the crater thickness accurately.

The final step in depth calibration is to find the time needed to sputter a particular crater to a known depth. A raw depth profile is shown in Figure 6. Each channel (or cycle number) on the abscissa is the time it takes to scan through the masses being measured. For example, if C^+, D^+, and H^+ are each measured for 1 s, then each cycle number is 3 s. Since the mass spectrometer requires a short time to switch between masses, each channel is actually slightly greater than 3 s. All secondary signals decrease when the cascade mixing region reaches the silicon substrate. The point of contact is accurately determined by observing the spot where a secondary ion current departs from its level plateau as shown in Figure 6. This channel number corresponds to the bilayer thickness (for this crater) minus the cascade mixing region.[61] The time scale is converted to one of depth after subtracting the TRIM 86 calculated cascade region thickness from each thickness. Figure 9 shows the data from Figure 6 converted to a linear count versus depth scale. Depth calibration in this manner avoids problems associated with assuming a constant sputtering rate and has a higher accuracy than the stylus technique.

Deconvolution: The true $c(z')$ and measured $I(z)$ concentration profiles are related by the convolution integral

$$I(z) = \int_{-\infty}^{\infty} c(z')\, g(z-z')\, dz' \tag{18}$$

The resolution function $g(z)$ can be obtained from the derivative of the measured profile[63] for a sharp interface. The depth resolution is twice the standard deviation of the response function.[37]

The solution to eq 18 is readily obtained if $I(z)$, $c(z)$, and $g(z)$ are all Gaussian functions. The true broadening Δz_0 is given in terms of the measured broadening Δz_m and the instrumental Gaussian broadening Δz_g by[63]

$$\Delta z_0 = (\Delta z_m{}^2 - \Delta z_g{}^2)^{1/2} \tag{19}$$

where

$$I(z) = \text{erf}\,(z/\Delta z_m) \tag{20}$$

$$c(z') = \text{erf}\,(z/\Delta z_0) \tag{21}$$

$$g(z-z') = \frac{1}{2\pi \Delta z_g{}^2} \exp\left[-2\left(\frac{z-z'}{\Delta z_g}\right)\right] \tag{22}$$

The resolution function Δz_g is assumed to be independent of depth. The true broadening, Δz_0, is obtained by correcting the measured broadening for the effect of the system response.

Other deconvolution methods must be used when the measured profile has a more general shape or when the resolution function cannot be approximated by a Gaussian probability function. Two approaches to obtain the general solution to eq 18 are the Fourier transform and van Crittert methods.[65-67] Comparison of the two procedures shows that convergence of the van Crittert method produces a solution equivalent to the best Fourier transform.[67]

The van Crittert method is an iterative procedure which gives the solution

$$c^i(z) = c^{i-1}(z) + I(z) - \int_{-\infty}^{\infty} c^{i-1}(z')\, g(z-z')\, dz' \tag{23}$$

$$c^0(z) \equiv I(z) \tag{24}$$

As n goes to ∞, $c^n(z)$ goes to $c(z)$. The applicability and convergence of this method has been examined in depth.[64,65,68,69] This is an excellent approach to recovering the true profile as long as $\Delta z_m \geq 2^{1/2}\, \Delta z_g$. When the depth resolution is greater than 70% of the measured profile, eq 23 may not converge to $c(z)$ in a realistic number of iterations.

Profile analysis program: A computer program was developed to deconvolute measured profiles and calculate various quantities. Sharp interface profiles were first analyzed to determine the depth resolution. The program locates the interface as the maximum of the derivative. To ensure accuracy, the raw profile is smoothed and the derivative is smoothed. The polynomial smoothing routine developed by Savitsky and Golay[71] was used. Comparison of the smooth and raw curves in Figure 10 indicates the usefulness of the polynomial routine. Derivatives are very sensitive to noise. The Savitsky and Golay method is applied to calculating derivatives in order to improve the signal to noise ratio. The smoothed derivative (Figure 11) from the profile in Figure 10 illustrates the success of polynomial smoothing. There is a compromise between noise reduction and deconvolution. Successive applications of the van Crittert procedure induces noise,[66] and iterative application of the polynomial smoothing produces convolution.[65] Smoothing of profiles used one iteration of a 25-point polynomial to achieve noise reduction (5X) and avoid convolution complications. Noise reduction is

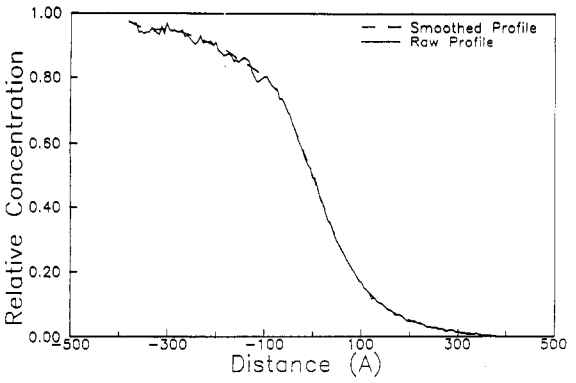

Figure 10. Result of the polynomial smoothing routine on a deuterium profile. The depth scale is now a relative distance based on the Matano interface (x and z of Figure 9 are equivalent).

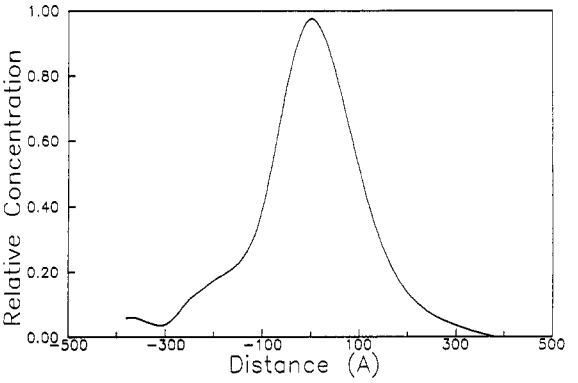

Figure 11. Derivative of the smoothed curve in Figure 10. The derivative was calculated by the polynomial smoothing routine used for the previous figure.

proportional to the square root of the number of points used in the polynomial fit.

Profiles from interdiffused bilayers were deconvoluted by using eq 18. Minor chain properties $N(t)$ and $X(t)$ were calculated from the deconvoluted profiles by using eqs 5 and 6. Diffusion coefficients at various concentrations were computed by the Matano–Boltzmann method by using eq 9.

Results

Interface design: A major objective of this study was to obtain the concentration depth profile at distances x, less than the radius of gyration R_g, of the polymer chains. At the reptation time τ, the average monomer interpenetration distance $X(\tau)$ for a symmetric polymer interface is given by Zhang and Wool as[21,75]

$$X(\tau) = 0.81R_g \tag{25}$$

R_g is given by

$$R_g = [C_\infty jM/6M_0]^{1/2}b_0 \tag{26}$$

where C_∞, j, M_0, and b_0 are the characteristic ratio, number of bonds per monomer, monomer molecular weight, and the bond length, respectively.

To observe small-scale motion at $t < \tau$ and $X(t) < X(\tau)$, $2X(t)$ must exceed the depth resolution $\Delta z \approx 150$ Å. For the 929K(HPS)/1082K (DPS) bilayer system, we calculate $X(\tau)$ as follows: M = 1 082 000, M_0 (deuterated) = 112, C_∞ = 10, b_0 = 1.54, and j = 2, such that R_g = 276 Å and $X(\tau)$ = 223 Å. Since the width of the interface is $2X(\tau)$ = 446 Å, this resolution should provide useful information in a considerable monomer interpenetration range at $t < \tau$.

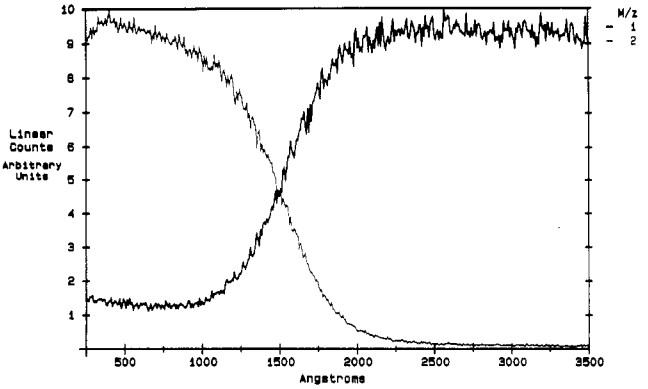

Figure 12. Protonated and deuterated depth profiles for a 1030K(DPS)/929K(HPS) interface healed at 146 °C for 720 min.

Table VI
Molecular Weight Series

anneal temp, °C	anneal time, min	mono-mers, counts·Å	interpene-tration distance, Å	first moment, counts·Å²	diffusion coefficient, cm²/s
(a) 93K(HPS)/111K(DPS) Results					
123.2	362	89.03	312	2.779×10^4	1.993×10^{-16}
128.2	90	51.29	258	1.326×10^4	4.657×10^{-16}
130.4	90	138.7	395	5.475×10^4	1.345×10^{-16}
132.4	90	217.5	550	1.196×10^5	2.664×10^{-15}
134.8	90	280.8	715	2.009×10^5	4.415×10^{-15}
140.0	30	256.9	700	1.798×10^5	1.245×10^{-14}
(b) 169K(HPS)/199K(DPS) Results					
125.4	362	45.13	218	9.824×10^3	1.403×10^{-16}
133.0	90	56.51	269	1.520×10^4	9.013×10^{-16}
135.8	90	90.17	351	3.168×10^4	1.719×10^{-15}
138.2	90	103.0	381	3.920×10^4	2.045×10^{-15}
146.6	30	137.8	443	6.102×10^4	8.611×10^{-15}
(c) 591K(HPS)/693K(DPS) Results					
138.2	362	34.35	140	4.794×10^3	2.026×10^{-16}
145.0	90	22.91	93	2.142×10^3	3.679×10^{-16}
151.5	90	90.18	252	2.272×10^3	3.099×10^{-15}
159.2	90	166.9	504	8.407×10^3	1.205×10^{-14}
166.2	90	203.6	628	1.279×10^3	1.777×10^{-14}
173.1	30	167.3	595	9.960×10^3	4.547×10^{-14}
(d) 929K(HPS)/1082K(DPS) Results					
142.0	362	38.77	127	4.932×10^3	1.522×10^{-16}
149.6	90	25.39	106	2.681×10^3	3.930×10^{-16}
153.2	90	45.83	171	7.853×10^3	1.117×10^{-15}
156.2	90	98.13	295	2.896×10^4	3.500×10^{-15}
160.2	90	82.37	312	2.572×10^4	3.866×10^{-15}
169.8	30	100.6	326	3.277×10^4	1.246×10^{-15}

Temperature dependence of diffusion: The diffusion coefficients D were first evaluated at long times ($t > \tau$) as a function of temperature and molecular weight. Figure 12 shows typical profiles obtained from the 1030K(DPS)/929K(HPS) bilayers at 146 °C and a 720-min diffusion time. The symmetry of the profiles permits a diffusion analysis from several sections. However, at short depths ($X \approx 500$ Å), the protonated profile may be contaminated with H from water vapor and the deuterated profile was used to extract the D values. D was calculated by using the Matano method for concentrations C, in the range $0.1 \leq C \leq 0.9$. The data (average D values) are summarized in Table VI.

The temperature dependence of D was analyzed by using both the Arrhenius and Vogel methods. Figure 13 shows a Vogel plot of log (D/T) vs $B/(T - T_\infty)$. The constants A and B from the Vogel analysis (eq 11) are given in Table VII for each bilayer and compared with data reported by Green et al.[76,77] using FRES. The FRES method measured $D = 8.8 \times 10^{-15}$ cm²/s for 900K(HPS)/915K(DPS) at 174 °C. Scaling to 1082K DPS using $D \propto M^2$, the value becomes D_{FRES}(1082K, 174 °C) = 6.29×10^{-15} cm²/s. Using Green's

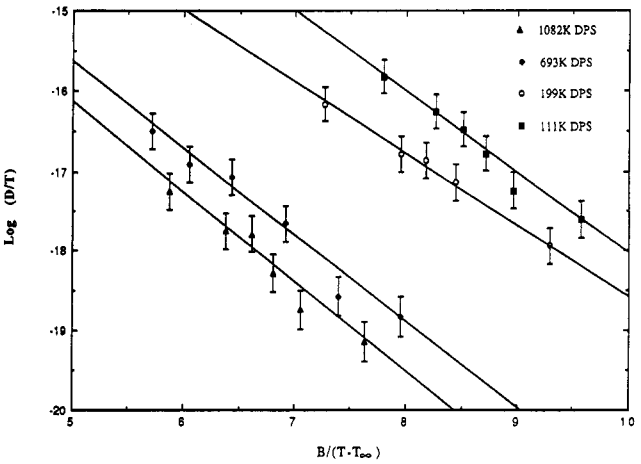

Figure 13. Diffusivities for all molecular weights fitted with the Vogel relation.

Table VII
Vogel Constants

	constant A		constant B	
mol wt	Kramer	exptl	Kramer	exptl
11K	-8.768	-7.531	710	753
199K	-9.2748	-9.8292	710	617
693K	-10.358	-10.194	710	778
1082K	-10.745	-10.490	710	808

A and B constants in Table VII, the Vogel analysis predicts D_{FRES}(1082K, 174 °C) = 1.72×10^{-14}, which is about 2.7 times larger than that obtained by scaling with molecular weight. The Vogel analysis for the 1082K sample using our values in Table VII predicts D_{SIMS}(1082, 174 °C) = 5.1×10^{-15} cm²/s, which is about 3.3 times smaller than Green et al.'s value.

At 170 °C, Green's constants are in better agreement with our experimental data (discussed for Figure 19). The comparison of data from two techniques involving considerable complexity can easily result in diffusion coefficients as a function of temperature and molecular weight, which may be off by several factors, typically ±2–5. However, the agreement in the order of magnitude between the data obtained by SIMS and FRES is considered to be satisfactory.

The data obtained from the Arrhenius method (eq 10) are summarized in Table VIII. The activation energy Q varies with each molecular weight because of the temperature range used for each bilayer. With bilayer samples of lower molecular weights, the healing temperatures were closer to T_g = 106 °C and thus the activation energies were higher, as expected.

Molecular weight dependence of diffusion at $t > \tau$: The self-diffusion coefficients D obtained at $t > \tau$ are shown as a function of molecular weight at 175 °C and compared with other techniques (from refs 55 and 56) in Figure 14. The data were shifted to a reference temperature of 175 °C. Using both the Vogel and Arrhenius method of shifting the data, the scaling laws at 175 °C are given by

$$D \propto M^{-2.1\pm0.2} \quad \text{(Vogel)} \tag{27}$$

$$D \propto M^{-2.1\pm0.2} \quad \text{(Arrhenius)} \tag{28}$$

with correlation coefficients of 0.976 and 0.952, respectively.

In Figure 14, the data were extrapolated to a reference temperature of 175 °C using an Arrhenius method with an activation energy of Q = 75 kcal/mol, as used by Tirrell.[55] This value is higher than Q values obtained by us at this temperature, but similar errors may have resulted in shifting the other data. However, the order of magnitude of the self-diffusion coefficients is correct and the agreement between SIMS and other methods in the same molecular weight range (10^5–10^6) is considered to be satisfactory.

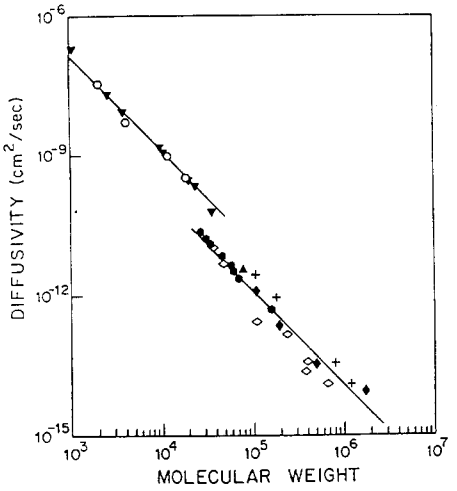

Polystyrene self-diffusion coefficient in cm²/s in the melt as a function of molecular weight at or near 175 °C; ▲ - data of Bueche et al.[112] (obtained at 237 °C via radiolabelling and reduced to 175 °C with Ea = 75 kJ/mol); ● - data of Antonietti et al.[112] (obtained via FRS at 177 °C); ◇ - data of Kramer et al.[119,149] (obtained via Rutherford backscattering at 170 °C); ◆ - data of Kumagai et al.[135] (obtained via radiolabelling at 150 °C and reduced to 175 °C with Ea = 75 kJ/mol); ▼ - data of Bacchus and Kimmich[146] (obtained via PGSE-NMR at 230 °C and reduced to 175 °C with Ea = 75 kJ/mol); ○ - data of Fleischer[147] (obtained via PGSE-NMR at or extrapolated to 175 °C). Lines drawn have slope of -2.

Figure 14. Comparison of diffusion coefficients measured by SIMS with other techniques.[55] Diffusivities are shifted to 175 °C by an Arrhenius relation using Q = 75 kcal/mol. SIMS values are denoted by the symbol (+) (with permission of Rubber Chemistry and Technology). Reproduced from ref 55.

Table VIII
Arrhenius Constants

mol wt (DPS)	D_0, cm²/s	Q, kcal/mol
111K	4.732×10^{30}	84.9
199K	1.768×10^{19}	64.2
693K	8.366×10^{15}	59.9
1082K	2.302×10^{16}	61.4

Diffusion coefficients at $t < \tau$: At times less than the reptation time and diffusion distances less than the radius of gyration, the chain configuration remain affected by the reflecting boundary condition imposed by the original surface. Interdiffusion at $t < \tau$ involves the relaxation of the nonequilibrium chain configurations.[18] Zhang and Wool[83] analyzed the short-time dynamics and its contribution to both Rouse and reptation relaxation processes. The "compressed" chain configurations have a rapid relaxation response in a region $t < T_{r0}$, where T_{r0} is the Rouse relaxation time for the entanglement length of molecular weight M_e. Segmental motion dominates the interdiffusion process for times $t < T_d$, where T_d is the Rouse relaxation time of the whole chain. For times $T_d < t < \tau$, the reptation mechanism is predicted to dominate the interdiffusion process. Since the monomer interdiffusion contains significant contributions from segmental motion of chains in nonequilibrium conformations, the diffusion coefficient D' should be considered apparent since it is not a measure of the true center-of-mass motion.

The apparent diffusion coefficients D' were measured for the 1082K(DPS)/929K(HPS) bilayer at $t < \tau$ and 146 °C. The reptation time at these conditions is about 317 min. Figure 15 shows D' versus healing time. The D' values decay from high values at $t < \tau$ to a constant value D_∞, at $t > \tau$. The high D' values at $t < \tau$ are largely due

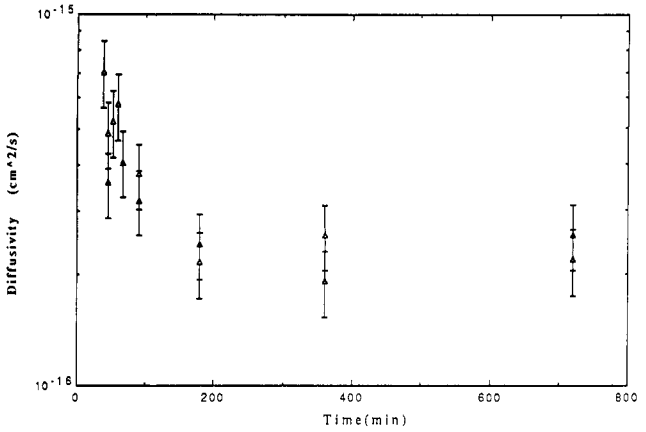

Figure 15. Diffusion coefficients as a function of time for 929K-(HPS)/1082(DPS) healed at 146 °C.

Table IX
Time Series Results of 929K(HPS)/1082K(DPS) Healed at 146.6 °C

anneal time, min	monomers, counts·Å	interpenetration depth, Å	first moment, counts·Å²	diffusion coefficient, 10^{-16} cm²/s
37.5	10.52	161	3499	7.047
45.0	15.99	114	3682	3.572
45.0	16.26	135	4609	4.865
52.5	14.66	164	3359	5.225
60.0	17.34	159	5130	5.785
67.5	10.72	146	6229	4.077
90.0	26.19	153	6651	3.195
90.0	43.50	166	7227	3.785
180.0	47.46	197	9329	2.430
180.0	47.22	180	8491	2.166
360.0	63.61	243	15490	1.925
360.0	75.49	277	20870	2.567
720.0	155.70	384	59750	2.565
720.0	107.10	364	38980	2.201

to segmental motion. Using Kramers' A and B constants (Table VII) in eq 11, $D_\infty = 3.7 \times 10^{-16}$ cm²/s, which is in close agreement with our data.

The relation between the surface-modified D' and bulk D_∞ can be approximated as follows. At $t = \tau$, the diffusion distance is on the order of the chain's end-to-end vector, R, such that $R^2 \propto D_\infty \tau$. At times $t < \tau$, the experimental interdiffusion diffusion distance $X(t)^2$, measured from the concentration profile, is related to the apparent diffusion coefficient by $X(t)^2 \propto D't$. Thus, the ratio of the apparent to the long-time diffusion coefficients is

$$D'/D_\infty = [X(t)^2/R^2]/(\tau/t) \tag{29}$$

It is readily shown from eq 29 that the ratio D'/D can be much greater than unity. Consider the time range $T_d < t < \tau$, where T_d is the Rouse relaxation time of the chain and is related to the reptation time via $\tau = 3M/M_e T_d$. The monomer diffusion function (from Table I) is $X(t)^2/R^2 = (t/\tau)^{1/2}$. Substituting in eq 29, the ratio of diffusion coefficients is obtained as

$$D'/D_\infty = (\tau/t)^{1/2} \quad (t \le \tau) \tag{30}$$

For example, referring to Figure 15 and Table IX, $\tau \approx$ 360 min. At $t \approx 37$ min, $(\tau/t)^{1/2} \approx 3$ and $D'/D \approx 7/2.2 \approx$ 3. Thus, in this time range, $D' \propto t^{-1/2}$ and a plot of log D' vs log t of the data in Table IX gives an approximate slope of $-1/2$, in agreement with the reptation theory. At the Rouse time, $D'/D = (3M/M_e)^{1/2}$; when $M = 10^6$ and M_e = 18 000, then $D'/D \approx 13$. At $t < T_d$, the ratio D'/D can be much larger.

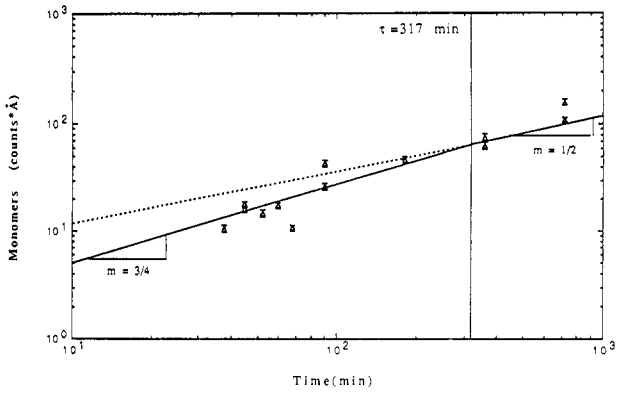

Figure 16. Monomers, N, crossing the interface as a function of time for 929K(HPS)/1082K(DPS) healed at 146 °C. The solid lines are drawn according to the reptation prediction such that $N \propto t^{3/4}$ at $t < \tau$ and $N \propto t^{1/2}$ at $t > \tau$, where $\tau = 317$ min. The dashed line is the extrapolated long-time slope of $1/2$ for comparison purposes.

The apparent self-diffusion coefficients shown in Figure 15 do not represent the actual center-of-mass motion. In fact, the opposite behavior occurs such that the real center-of-mass diffusion coefficient D is less than the equilibrium value at distances $X(t) < R_g$. The relaxation of the compressed configurations results in very little displacement of the chain's center of mass,[18] $X(t)_{cm}$. Since $X(t)_{cm} \approx 0$ and $D \propto X(t)_{cm}^2/t$, then we expect $D \ll D_\infty$ at $t < \tau$. This behavior is largely dependent on the static rather than the dynamic properties of the chains and should be observed for Rouse as well as reptation-controlled diffusion.

Number of monomers diffused $N(t)$ at $t < \tau$: The number of monomers $N(t)$ crossing the interface plane is determined from the integral of the concentration profile (eq 5). Figure 16 shows a plot of log $N(t)$ versus log t for the 929K/1082K bilayer at 146.6 °C. The reptation time τ was calculated by using[1]

$$\tau = R^2/(3\pi^2 D) \tag{31}$$

where D is measured at $t \gg \tau$.

The self-diffusion coefficient D was obtained by the method suggested by Zhang and Wool[21,75] using measured $N(t)$ values under Fickian diffusion conditions at long times via

$$D = \pi N^2(t)/t \tag{32}$$

for $t > \tau$. Note that the proportionality constant in the relation $N(t) \propto t^{1/2}$ at $t > \tau$ is $(D/\pi)^{1/2}$. Using eq 32 and the $N(t)$ experimental data in Table IX, we obtain $D \approx 0.83 \times 10^{-16}$ cm²/s for $t \ge 360$ min. Substituting for D and R = 677 Å in eq 31, we obtain $\tau \approx 317$ min.

The average value of D (Table IX) at $t \ge 360$ min is D = 2.3×10^{-16} cm²/s. This value gives $\tau = 112$ min, which is nearly 3 times smaller than τ obtained by eq 32. We use the value of $\tau = 317$ min because the data in Figure 15 and subsequent figures do not show asymptotic behavior at 112 min but closer to 300 min. The method used by Zhang and Wool is internally consistent and not subject to potential boundary effects and nonasymptotic behavior of D vs time in Figure 15. The D values obtained by both methods are within the data scatter previously discussed.

In Figure 16, the theoretical slopes of $1/2$ and $3/4$ from eqs 1 and 2 are shown for ease of comparison with the reptation predictions. At $t > \tau$, the data are expected to be in accord with $N(t) \propto t^{1/2}$, as would be predicted by the normal Fickian diffusion process. At $t < \tau$, the data deviate from the extrapolated $t^{1/2}$ plot (dotted line, Figure 16). A

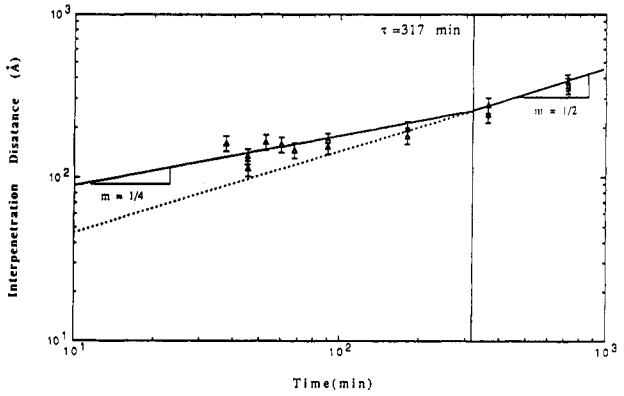

Figure 17. Average interpenetration distance, X, as a function of time for 929K(HPS)/1082K(DPS) healed at 146 °C. The transition in slope from $^1/_4$ to $^1/_2$ at $t = \tau$ is drawn in accordance with the reptation prediction.

least-squares fit of the data in the range $t \leq 360$ min gives

$$N(t) \approx 0.63t^{0.815} \tag{33}$$

which compares with the reptation prediction $N(t) \propto t^{0.75}$. The data in Figure 16 can be fitted with a power law, $N(t) = 0.66t^{0.8}$ in the entire data range $0 < t < 720$ min and by $N(t) = 1.817t^{0.63}$, in the range $90 \leq t \leq 720$ min. This result is supportive of the predicted slope transition from $t^{3/4}$ to $t^{1/2}$ at the reptation time.

The number of monomers diffused at the reptation time $N(\tau)$ is obtained from eqs 31 and 32 as

$$N(\tau) = (2/\pi^3)^{1/2}R_g \tag{34}$$

or, roughly, $N(\tau) \approx R_g/4$. Since $R_g = 276$, $N(\tau) = 70$ Å, which compares with the data in both Figure 16 and eq 33, where $N(317) = 69$ Å.

Monomer interdiffusion at $t < \tau$: The average monomer interpretation distance, $X(t)$, was measured from the normalized first moment of the concentration profile eq 6 and is given in Table IX. The experimental uncertainty was on the order of 11%. To compare with the scaling law predictions (eqs 3 and 4), we plotted log $X(t)$ vs log t as shown in Figure 17. Again, at $t > \tau$, $X(t) \propto t^{1/2}$ as expected for normal Fickian diffusion. At $t < \tau$ where $\tau \approx 317$ min, the data deviate from the extrapolated $t^{1/2}$ slope and lie closer to the theoretical $t^{1/4}$ slope. A least-squares fit of the data for $0 < t \leq 360$ min gives

$$X(t) = 49.9t^{0.27} \tag{35}$$

which compares favorably with the reptation prediction.

Over the entire healing range, $0 < t \leq 720$ min, we obtain $X(t) = 38.5t^{0.33}$. In the range $180 \leq t \leq 720$ min, we have $X(t) = 14.3t^{0.50}$. Thus, at short times the data are well represented by $X(t) \propto t^{1/4}$, which changes to $X(t) \propto t^{1/2}$ at long times. These results provide good support for the reptation predictions. The uniqueness of these results and the applicability of similar relations to Rouse diffusion of chains at interfaces are being investigated by Zhang and Wool.[83]

A further comparison of theory with experiment is obtained from the static prediction that the average monomer interpenetration distance at the reptation time is given by $X(\tau) = 0.81R_g$. Given that $\tau = 317$ min, we obtain from eq 35 that $N(317) = 233.55$ Å. This compares with $R_g = 276$ Å and $0.81R_g = 223$ Å. In Figure 17, the crossover in diffusion behavior in the vicinity of $R_g = 223$ Å is consistent with this prediction.

Using eq 35, the interdiffusion distance at the Rouse time $T_d = 2$ min is obtained as $X(T_d) = 60$ Å. The latter value is comparable to the "tube" diameter of the reptation model, as discussed by Graessley.[73] The tube diameter R_{tube} should be comparable to the end-to-end vector R_e of the entanglement molecular weight, M_e. With $R_{tube} = 1.31R$ (the factor 1.31 is used to describe the diameter of the sphere which completely contains the entire chain of end-to-end vector R), $M_e = 18\,000$, $R_e = 90$ Å, and $R_{tube} = 118$ Å. If $X(T_d) = R_{tube}/2$ because of symmetry at the interface, then $R_{tube}/2 = 59$ Å, which is in agreement with the interdiffusion inferred at the Rouse time.

The above results were obtained with the assumption that the chain ends were uniformly distributed in space. de Gennes[84] has suggested that the chain ends may separate at the surface and alter the interdiffusion process in a more complex manner. However, if the chain ends were predominantly at the interface plane at $t = 0$, the scaling law for $X(t)$ would not change to time dependence but $N(t) \sim t^{1/2}M^{-1}$. The intermediate situation needs further attention, in terms of both polydispersity and the spatial distribution of chain ends from a particular molecular weight fraction.

The above SIMS results are consistent with recent studies of interdiffusion in symmetric HPS/DPS interfaces using specular neutron reflection (SNR) methods by Karim and Felcher et al.[85,88] and by Zhang and Wool et al.[83,86] The advantage of the SNR method is that it is nondestructive and has an intrinsic depth resolution of about 5 Å. The disadvantage of the SNR technique is that the concentration profile is obtained by deconvolution of the reflectance spectrum and the nonuniqueness of the calculated concentration profile may pose a problem.

Recently, Steiner et al.[81] examined the formation of a HPS/DPS interface using forward scattering (FRES) from nuclear reactions produced by a ^{3}He beam from a Van der Graaff accelerator. The molecular weights of the DPS and HPS polymers were 1.03×10^6 and 2.89×10^6, respectively. They observe that the width $w(t)$ of the interface increases approximately as $w(t) \propto t^{0.34}$ at 160 °C, which they interpret in terms of the diffusion of partially miscible polymers (TSD). At 160 °C, the interface broadened up to 1000 Å and remained constant at times greater than 50 000 s (833 min), which is consistent with the TSD effect. These times are much greater than the reptation time. At 140 °C, they obtained $w(t) \propto t^{0.27}$, up to times of 10^6 s. At this temperature an upper depth plateau indicating restricted growth of the interface was not observed in the depth range studied. The data are not sufficiently detailed in the region of the reptation time and depths less than the radius of gyration to determine if the transition in slope from $^1/_4$ to $^1/_2$ occurs before the onset of TSD.

Miscibility of DPS in HPS. With high molecular weight HPS/DPS systems, Bates et al.[31] demonstrated that phase separation can occur if $\chi(T) > \chi_{cr}$. Since our molecular weights are high, the potential exists for both phase separation and thermodynamic slowing down of diffusing chains. With equal molecular weights, $\chi_{cr} = 2/N$ from eq 13. Since $N = 10^4$, $\chi_{cr} = 2.0 \times 10^{-4}$. The temperature dependence of the Flory–Huggins interaction parameters is given by Bates et al.[31] as

$$\chi(T) = 0.2/T\,\text{K} - 2.9 \times 10^{-4} \tag{36}$$

At $T = 419.2$ K (146 °C), $\chi(146) = 1.87 \times 10^{-4}$. Since $\chi(T) < \chi_{cr}$, we expect that DPS is miscible in HPS under these conditions. This expectation is supported by the experimental results where diffusion at distances greater than the radius of gyration of the polymers was observed by SIMS. However, we should be concerned with "ther-

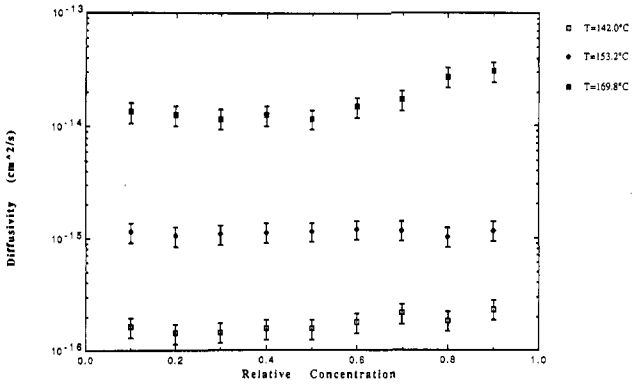

Figure 18. Diffusion coefficients from 929K(HPS)/1082K(DPS) as a function of temperature at three temperatures, investigating thermodynamic slowing down at the critical concentration of $c = 0.49$.

modynamic slowing down" (TSD) since eq 36 only considers the equilibrium miscibility criterion. The molecular weights used by Steiner et al.[81] were such that $\chi(T) > \chi_{cr}$ at several temperatures, including 140 °C, and the TSD effect was observed at diffusion distances on the order of 1000 Å.

Our experimental design was different from that used by Green and Doyle,[34] who reported the TSD effect using FRES. Their approach utilized bilayer samples with slightly different compositions (10%), and they assumed that D was independent of composition for their analysis. They find that the diffusion coefficient decreases at the critical concentration $c_{cr} = 0.5$, which is indicative of the TSD effect. The decrease in D is amplified with decreasing temperature. The mutual diffusion coefficient measured at c_{cr}, $D(c_{cr})$, is deduced from eqs 13–16 as

$$D(c_{cr}) = D^*[1 - \chi(T)/\chi_c] \quad (37)$$

where D^* is the self-diffusion coefficient in the absence of TSD. For our SIMS experiments with $M = 10^6$ and $T = 146$ °C, $D/D^* = 0.065$ and we could expect a large TSD effect.

Our results are shown in Figure 18 for $M = 10^6$ and welding temperatures of 142–170 °C at times $t > \tau$. These plots are representative of the other test temperatures. The large TSD effect that was anticipated in the vicinity of c_{cr} (eq 37) was not observed but is expected to occur at longer diffusion distances. The distances explored by the SIMS method in this work were too short for the composition fluctuations to develop and slow the interdiffusion. The enhanced diffusion due to segmental motion (Figure 15) at $t < \tau$ further supports our conclusions. Recent experiments with neutron reflection analysis of HPS/DPS blend interfaces by Karim and Felcher et al.[87,88] also failed to detect the TSD effect for deuterated/protonated blends of PS with varying compositions. Again, the depth range ($x < 500$ Å) in their study was comparable to that used in our SIMS study. The lack of a TSD effect in both the SIMS and neutron reflection studies is most fortunate in terms of designing and interpreting short-range interdiffusion data.

Summary

In this paper, we outlined the details of the SIMS method to measure interdiffusion at polystyrene symmetric DPS/HPS interfaces. The following points are made in summary:

(1) The SIMS method provides the concentration profiles with a depth resolution of ca. 135 Å.

(2) The SIMS method permitted a relatively easy measurement of the self-diffusion coefficient D, with minimal data processing. At long times, the raw SIMS data can be directly analyzed to obtain D values. At short times and distances ($x < R_g$) deconvolution procedures improved the quality of the data.

(3) The molecular weight dependence of the self-diffusion coefficient was found to scale as $D \propto M^{-2}$, in agreement with other methods.

(4) At short times, the apparent self-diffusion coefficient was greater than the long-time equilibrium value. This result could be interpreted as the segmental motion contribution to monomer interdiffusion since little center-of-mass motion occurs at distances less than the radius of gyration.

(5) The short-time results for both the number of monomers crossed ($N(t) \propto t^{3/4}$) and the average monomer interpenetration distance ($X(t) \propto t^{1/4}$) were in good agreement with the reptation scaling law predictions for the static and dynamic properties of polymer melts.

(6) The thermodynamic slowing down due to the deuterium isotope effect was not observed in the SIMS experiment in the depth range explored, $x < 500$ Å.

(7) The SIMS results at $x < R_g$ are consistent with results of similar symmetric interface diffusion studies using neutron reflection at Argonne National Laboratory.

Acknowledgment. We are grateful to the National Science Foundation for financial support of this work with Grants DMR 86-11551 (Polymers Program) and DMR 86-12860 (Materials Research Laboratory). Additional support for the SIMS facility was obtained through the Center for Microanalysis of Materials at MRL with Grant DE-AC02-76ERD1198. Appreciation and thanks are given to Dr. Chris Loxton and Ms. Judy Baker for many useful discussions and technical assistance with the SIMS facility.

References and Notes

(1) de Gennes, P.-G. *J. Chem. Phys.* **1971**, *55*, supplement 2, 572.
(2) Doi, M.; Edwards, S. F. *J. Chem. Soc., Faraday Trans. 2* **1978**, *74*, 1789.
(3) Doi, M.; Edwards, S. F. *J. Chem. Soc., Faraday Trans. 2* **1978**, *74*, 1802.
(4) Doi, M.; Edwards, S. F. *J. Chem. Soc., Faraday Trans. 2* **1978**, *74*, 1818.
(5) Doi, M.; Edwards, S. F. *J. Chem. Soc., Faraday Trans. 2* **1979**, *75*, 38.
(6) Green, P. F.; Mills, P. J.; Palstrom, C. J.; Mayer, J. W.; Kramer, E. J. *Phys. Rev. Lett.* **1984**, *53*, 2145.
(7) Green, P. F.; Mills, P. J.; Palstrom, C. J.; Mayer, J. W.; Kramer, E. J. *Appl. Phys. Lett.* **1984**, *45*, 957.
(8) Klein, J.; Briscoe, B. J. *Proc. R. Soc. London* **1979**, *53*, A365.
(9) Klein, J.; Fletcher, D.; Fetters, L. J. *Nature (London)* **1983**, *304*, 526.
(10) Bartles, C. R.; Graessley, W. W.; Crist, B. J. *J. Polym. Sci., Polym. Lett. Ed.* **1983**, *21*, 495.
(11) Summerfield, G. C.; Ullman, R. *Macromolecules* **1987**, *20*, 401.
(12) Russell, T. P.; Karin, A.; Mansour, A.; Felcher, G. P. *Macromolecules* **1988**, *21*, 1890. Russell, T. P., private communication. Symposium on Light, X-Ray and Neutron Scattering and Reflection from Polymers, 200th Meeting of the American Chemical Society, Washington, DC, Aug 1990.
(13) Jones, R. A. L.; Kramer, E. J.; Rafailovich, M. H.; Sokolov, J.; Schwarz, S. A. *Phys. Rev. Lett.* **1989**, *62*, 280.
(14) Composto, R. J.; Stein, R. S.; Kramer, E. J.; Jones, R. A. L.; Mansour, A.; Karim, A.; Felcher, G. P. *Phys. B* **1989**, *156–157*, 434.
(15) Whitlow, S. J.; Wool, R. P. *Macromolecules* **1989**, *22*, 2648.
(16) Doi, M.; Edwards, S. F. *The Theory of Polymer Dynamics*; Clarendon Press: Oxford; 1986.
(17) Wool, R. P. *J. Elast. Plast.* **1985**, *17*, 106.
(18) Kim, Y. H.; Wool, R. P. *Macromolecules* **1983**, *16*, 1115.
(19) Wool, R. P.; Yuan, B.-L.; McGarel, O. J. *Polym. Eng. Sci.* **1989**, *29*, 1340.

(20) de Gennes, P.-G. *Scaling Concepts in Polymer Physics* Cornell University Press: Ithaca, NY; 1979.
(21) Zhang, H.; Wool, R. P. *Macromolecules* **1989**, *22*, 3018.
(22) de Gennes, P.-G. *C. R. Acad. Sci., Ser. B* **1980**, *291* (Nov), 219.
(23) de Gennes, P.-G.; Leger, L. *Annu. Rev. Phys. Chem.* **1982**, *33*, 49.
(24) Wool, R. P.; O'Connor, K. M. *J. Appl. Phys.* **1981**, *52*, 5194.
(25) Reed-Hill, R. E. *Physical Metallurgy Principles*, 2nd ed.; Litten Educational, Brooks/Cole Engineering Division: Monterey, CA; 1973.
(26) Matano, C. *Jpn. J. Phys.* **1932**, *8*, 109.
(27) Kramer, E. J.; Green, P.; Palmstrom, C. J. *Polymer* **1984**, *25*, 473.
(28) Wan, W.; Whittenburg, S. L. *Macromolecules* **1986**, *19*, 925.
(29) Kline, D. B.; Wool, R. P. *Polym. Eng. Sci.* **1988**, *28*, 52.
(30) Green, P.; Kramer, E. J. *J. Mater. Res.* **1986**, *1*, 202.
(31) Bates, F. S.; Wignall, G. D.; Koehler, W. C. *Phys. Rev. Lett.* **1985**, *55*, 2425.
(32) Bates, F. S.; Wignall, G. D. *Macromolecules* **1986**, *19*, 934.
(33) Green, P. F.; Doyle, B. L. *Phys. Rev. Lett.* **1986**, *57*, 2407.
(34) Green, P. F.; Doyle, B. L. *Macromolecules* **1987**, *20*, 2471.
(35) Katz, W.; Newman, J. G. *MRS Bull.* **1987**, *12*, 40.
(36) Magee, C. W.; Honig, R. E. *Surf. Interface Anal.* **1982**, *4*, 35.
(37) Benninghoven, A.; Rudenaur, F. G.; Werner, H. W. *Secondary Ion Mass Spectroscopy*; Chemical Analysis Series 86; John Wiley and Sons: New York, 1987.
(38) *New Characterization Techniques for Thin Polymer Films*; Eds. Tong, H.-M. Nguyen, L. T., Eds.; Wiley-Interscience: New York, 1990.
(39) Green, P. F.; Doyle, B. L. Reference 38, Chapter 6.
(40) Sigmund, P. In *Secondary Ion Mass Spectroscopy SIMS IV*; Benninghoven, A., et al., Eds.; Springer Series in Chemical Physics 36; Springer-Verlag: Berlin, 1984.
(41) Williams, P. In *Applied Atomic Collision Physics*; Datz, S., Ed.; Academic Press: New York, 1983; Vol. 4.
(42) Biersak, J. P. Beam Modification of Materials. In *Ion Beam Modification of Insulators*; Mazzoldi, P., Arnold, G. W., Eds.; Elsevier: New York, 1987; Vol. 2.
(43) Hofmann, S. *Surf. Interface Anal.* **1980**, *4*, 148; **1980**, *2*, 56.
(44) Briggs, D.; Wooton, A. B. *Surf. Interface Anal.* **1982**, *4*, 109. Briggs, D. *Surf. Interface Anal.* **1986**, *9*, 391.
(45) Wittmack, K. *Nucl. Instrum. Methods* **1980**, *168*, 343.
(46) Chujo, R.; Nishi, T.; Sumi, Y.; Adachi, T.; Naito, H.; Frentzel, H. *J. Polym. Sci., Polym. Lett. Ed.* **1983**, *21*, 487; *Bull. Inst. Chem. Res. (Kyoto Univ.)* **1988**, *66*, 312.
(47) Valenty, S. J.; Chera, J. J.; Olson, D. R.; Webb, K. K.; Smith, G. A.; Katz, W. *J. Am. Chem. Soc.* **1984**, *106*, 6155.
(48) Anderson, H. H. *Appl. Phys.* **1979**, *18*, 131.
(49) Biersak, J. P. *Nucl. Instrum. Methods* **1981**, *182/183*, 199.
(50) Hofmann, S. *Secondary Ion Mass Spectroscopy SIMS III*; Benninghoven, A., et al., Eds.; Springer Series in Chemical Physics 19; Springer-Verlag: Berlin, 1982.
(51) Sigmund, P.; Gras-Marti, A. *Nucl. Instrum. Methods* **1980**, *168*, 389.
(52) Hofer, W. O.; Littmark, U. *Secondary Ion Mass Spectrometry SIMS III*; Benninghoven, A.; et al., Eds.; Springer Series in Chemical Physics 19; Springer-Verlag: Berlin, 1982.
(53) Wittmack, K. *Nucl. Instrum. Methods* **1985**, *B7/8*, 750.
(54) Williams, P.; Baker, J. E. *Nucl. Instrum. Methods* **1981**, *182/183*, 15.
(55) Tirrell, M. *Rubber Chem. Technol.* **1984**, *57*, 523.
(56) Kausch, H. H.; Tirrell, M. *Annu. Rev. Mater. Sci.* **1989**, *19*, 341.
(57) Kern, W. *RCA Eng.* **1983**, *28*, 99. Kern, W.; Puotinen, D. A. *RCA Rev.* **1970**, *187*.
(58) Henderson, R. C. *J. Electrochem. Soc.: Solid-State Sci. Technol.* **1972**, *119*, 772.
(59) Hess, M., Hamburg, H. R., Morgans, W. M. Eds. *Hess's Paint Film Defects: Their Causes and Cure*, 3rd ed.; Chapman-Hall: London, 1979.
(60) Riedling, K. *Ellipsometry for Industrial Applications*; Springer-Verlag: New York, 1988.
(61) Tsong, I. S. T.; Monkowski, J. R.; Hoffman, D. W. *Nucl. Instrum. Methods* **1985**, *B7/8*, 750.
(62) Werner, H. W. *Surf. Interface Anal.* **1982**, *4*, 1.
(63) Hall, P. M.; Morabito, J. M.; Panousis, N. T. *Thin Solid Films* **1977**, *41*, 341.
(64) Hofmann, S.; Sanz, J. M. *Thin Film and Depth Profile Analysis*; Oechsner, H., Ed.; Springer-Verlag: Berlin, 1984.
(65) Carley, A. F.; Joyner, R. W. *J. Electron Spectrosc. Relat. Phenom.* **1979**, *16*, 1.
(66) van Crittert, P. H. *Z. Phys.* **1931**, *69*, 298 (English translation).
(67) Wertheim, G. K. *J. Electron. Spectrosc. Relat. Phenom.* **1975**, *6*, 239.
(68) Madden, H. H.; Houston, J. E. *J. Appl. Phys.* **1976**, *47*, 3071.
(69) Ho, P. S.; Lewis, J. E. *Surf. Sci.* **1976**, *55*, 335.
(70) Whitlow, S. J. M.S. Thesis, University of Illinois, Urbana, IL, 1989.
(71) Savitsky, A.; Golay, M. J. E. *Anal. Chem.* **1964**, *36*, 1627.
(72) Steiner, J.; Termonia, Y.; Deltour, J. *Anal. Chem.* **1972**, *44*, 265.
(73) Graessley, W. W. *Advances in Polymer Science*; Springer-Verlag: Berlin, 1982; Vol. 47.
(74) Walczak, W. J. M.S. Dissertation, University of Illinois, Urbana, IL, 1989.
(75) Zhang, H.; Wool, R. P. *Macromolecules*, in press.
(76) Green, P. F.; Kramer, E. J. *Macromolecules* **1986**, *19*, 1108.
(77) Green, P. F. Ph.D. Thesis, Cornell University Press: Ithaca, NY, 1984.
(78) Composto, R. J. Ph.D. Thesis, Cornell University Press: Ithaca, NY, 1987.
(79) DiBenedetto, A. T.; Scola, D. A. *J. Colloid Interface Sci.* **1978**, *64*, 480.
(80) Coulon, G.; Russell, T. P.; Deline, V. R.; Green, P. F. *Macromolecules* **1989**, *22*, 2581.
(81) Steiner, U.; Krausch, G.; Schatz, G.; Klein, J. *Phys. Rev. Lett.* **1990**, *64*, 1119.
(82) Ferry, J. D. *Polymer Viscoelastic Properties*; John Wiley: New York, 1970.
(83) Zhang, H.; Wool, R. P. *Concentration Profiles at Amorphous Polymer Interfaces. Polymer Preprints of the American Chemical Society*, Aug 1990, American Chemical Society: Washington, DC; *Macromolecules*, in press.
(84) de Gennes, P.-G. *C. R. Acad. Sci. Paris* **1988**, *307*, 1841.
(85) Karim, A.; Mansour, A.; Felcher, G. P.; Russell, T. P. *Phys. Rev. Lett. B* **1990**, *42* (10), 6846.
(86) Zhang, H.; Foster, K. L.; Wool, R. P.; Karim, A.; Felcher, G. P. *Macromolecules*, in press.
(87) Felcher, G. P., private communication.
(88) Karim, A. Ph.D. Thesis, Northwestern University, Evanston, IL, 1990.

Registry No. PS, 9003-53-6.